The $(CN_3H_6)_4[Zn_3(SeO_3)_5]$ structure is completely different to those of previously characterized "inorganic" zinc selenites, all of which contain a dense network of ZnO_6 octahedra and $(H)SeO_3$ pyramids.[10] The 12-ring templating effect of the C2-centered guanidinium cation may be likened to its effect in templating polyhedral 12-rings (six ZnO_4 and six PO_4 tetrahedra) in zincophosphate (ZnPO) frameworks,[11] although the overall structures of the ZnPO materials are completely different to that of the title compound. $(CN_3H_6)_4[Zn_3(SeO_3)_5]$ is the first member of a family of organically templated selenites which we will describe in more detail in the near future.

Experimental Section

Synthesis: Guanidinium carbonate (1.80 g, 10 mmol), ZnO (0.81 g, 10 mmol), SeO_2 (2.22 g, (20 mmol), and H_2O (20 mL) were added to a PTFE bottle, shaken well, and placed in a 95 °C oven. The bottle was vented and recapped after 1 h. An essentially quantitative yield of intergrown transparent slabs (longest dimension up to 1 mm) of $(CN_3H_6)_4[Zn_3(SeO_3)_5]$ was recovered by vacuum filtration after 7 days.

Properties: A simulation based on the $(CN_3H_6)_4[Zn_3(SeO_3)_5]$ single-crystal structure was in excellent agreement with X-ray powder data, indicating phase purity and high crystallinity. Thermogravimetric analysis/differential thermal analysis (TGA/DTA) (ramp at 10 °K min^{-1} to 900 °C in air) for $(CN_3H_6)_4[Zn_3(SeO_3)_5]$ revealed the onset of a multistage 72 % weight loss at ~200 °C, which was complete by ~580 °C. Strong endothermic transitions at ~205, ~270, and ~570 °C were apparent. The weight loss of ~23 % occurring between ~200 °C and ~280 °C probably corresponds to loss of the guanidine template molecules (calcd 22.0 %). The overall weight loss is in fair agreement with a scheme involving the loss of all the organic species and selenium (as SeO_2) to result in a residue of $3 \times ZnO$ (calcd 77 %). The FTIR spectrum for $(CN_3H_6)_4[Zn_3(SeO_3)_5]$ revealed strong peaks at 3344 and 1671 cm^{-1}, corresponding to guanidinium N–H stretches and C–N/C=N stretches, respectively. Elemental analysis was satisfactory (%): calcd: C 4.48, H 2.26, N 15.69; found: C 4.11, H 2.23, N 14.59.

Structure determination: A crystal of $(CN_3H_6)_4[Zn_3(SeO_3)_5]$ (broken fragment, dimensions $\sim 0.27 \times 0.12 \times 0.11$ mm) was selected for data collection on a Bruker SMART 1000 CCD diffractometer (graphite-monochromated $Mo_{K\alpha}$ radiation, $\lambda = 0.71073$ Å, $T = 300$ K): orthorhombic cell parameters from 4753 reflections ($4.6° < 2\theta < 50°$), 16466 reflections scanned ($2° < 2\theta < 50°$). After merging ($R_{Int} = 0.055$), 1830 of the 2429 unique reflections were considered observed [$I > \sigma(I)$]. An absorption correction was applied with SADABS[12] (min., max. equivalent transmission factors = 0.496, 0.862). The structure was solved by direct methods using SHELXS,[13] refined by full-matrix least squares using CRYSTALS,[14] and illustrated using ORTEP[15] and ATOMS.[16] Hydrogen atoms associated with the guanidinium cations were placed geometrically and refined by riding. Final residuals: $R(F) = 0.026$, $R_w(F) = 0.028$.

Crystal data: $(CN_3H_6)_4[Zn_3(SeO_3)_5]$, $M_r = 1071.25$, orthorhombic, space group *Pbcm* (no. 57), $a = 8.9007(4)$, $b = 15.0771(7)$, $c = 20.5096(9)$ Å, $V = 2752.3(4)$ Å^3, $Z = 4$, $\mu = 92.9$ cm^{-1}, $\rho_{calcd} = 2.586$ g cm^{-3}, $F(000) = 2048$. Further details on the crystal structure investigation may be obtained from the Fachinformationszentrum Karlsruhe, 76344 Eggenstein-Leopoldshafen, Germany (fax: (+49) 7247-808-666; e-mail: crysdata@fiz-karlsruhe.de), on quoting the depository number CSD-411298.

Received: May 15, 2000 [Z15124]

[1] A. K. Cheetham, G. Férey, T. Loiseau, *Angew. Chem.* **1999**, *111*, 3466; *Angew. Chem. Int. Ed.* **1999**, *38*, 3268.
[2] M. E. Davis, R. F. Lobo, *Chem. Mater.* **1992**, *4*, 756.
[3] M. I. Khan, L. M. Meyer, R. C. Haushalter, A. L. Schweizer, J. Zubieta, J. L. Dye, *Chem. Mater.* **1996**, *8*, 43.
[4] S. Natarajan, A. K. Cheetham, *J. Solid State Chem.* **1998**, *140*, 435.
[5] R. J. Francis, M. J. Drewitt, P. S. Halasyamani, C. Ranganathachar, D. O'Hare, W. Clegg, S. J. Teat, *Chem. Commun.* **1998**, 279.
[6] X. Bu, P. Feng, G. D. Stucky, *J. Am. Chem. Soc.* **1998**, *120*, 11 204.
[7] M. Shieh, K. J. Martin, P. J. Squattrito, A. Clearfield, *Inorg. Chem.* **1990**, *29*, 958.
[8] G. Geister, *Z. Kristallogr.* **1998**, *213*, 266.
[9] Z. Bircsak, W. T. A. Harrison, *Inorg. Chem.* **1998**, *37*, 5387.
[10] W. T. A. Harrison, *Acta Crystallogr. Sect. C* **1999**, *55*, 1980.
[11] W. T. A. Harrison, M. L. F. Phillips. *Chem. Mater.* **1997**, *9*, 1837.
[12] Program SADABS, Bruker AXS Inc., Madison, Wisconsin, USA, **1999**.
[13] G. M. Sheldrick, SHELXS86 user guide, University of Göttingen, Germany, **1986**.
[14] D. J. Watkin, J. R. Carruthers, P. W. Betteridge, CRYSTALS user guide, Chemical Crystallography Laboratory, University of Oxford, UK, **1999**.
[15] L. J. Farrugia, *J. Appl. Crystallogr.* **1997**, *30*, 565.
[16] Program ATOMS, Shape Software Inc., Kingsport, Tennessee, USA, **1999**.

Correlation of the Topology of the Electron Density of Pyrite-Type Transition Metal Sulfides with Their Catalytic Activity in Hydrodesulfurization**

Yosslen Aray,* Jesus Rodriguez, David Vega, and Eloy Nouel Rodriguez-Arias

Transition metal sulfides (TMSs) are an important class of catalysts that are stable under the severe conditions of sulfo-reductive hydroprocessing of petroleum-based feedstocks.[1, 2] Systematic experimental[2, 3] and theoretical[2–5] studies on the hydrodesulfurization (HDS) activity towards dibenzothiophene (DBT) of various metal sulfide catalysts have shown that the strength of the metal–sulfur bonding plays an important role in the HDS process. Two different models for assessing the M–S bond strength have been developed.[2, 5] In the model developed by Topsøe et al.,[2] the M–S bond energy is obtained from the bulk modulus of the metal and the degree of filling of the TMS d band (calculated by ab initio methods). This model predicts that HDS activity is inversely correlated with M–S bond strength. Hence, the highest activity is

[*] Y. Aray
Centro de Quimica
IVIC, Apartado 21827
Caracas 1020 A (Venezuela)
Fax: (+58) 2-504-1350
E-mail: yaray@quimica.ivic.ve
J. Rodriguez
Centro de Quimica
IVIC, Caracas (Venezuela)
D. Vega
FACYT, Universidad de Carabobo, Valencia (Venezuela)
E. N. Rodriguez-Arias
Laboratorio de Modelaje en Catalisis
Departamento de Química, Universidad Simón Bolivar
Caracas (Venezuela)

[**] The authors acknowledge CONICIT of Venezuela (Projects S1-95001616 and S1-2673) for providing funding for the SGI ORIGIN 2000 and SGI O2 workstations used in this work.

  1433-7851/00/3921-3810 $ 17.50+.50/0

observed for TMSs that possess the most weakly bound sulfur atoms at the surface. In the model developed by Toulhoat et al.,[5] the M–S bond strength is estimated as the bulk cohesive energy (experimental or calculated by ab initio methods) per formula unit divided by the number of TM–S bonds. Using this model gives a typical "volcano" plot for the correlation between HDS activity and the metal–sulfur bond strength. This suggests the existence of an optimum M–S bond strength. This result was interpreted in the spirit of the Sabatier principle:[6] solids whose heats of formation and hence whose metal–sulfur bond strengths are too large or too small are practically inactive, while those with intermediate M–S bond strengths are active. Pyrite-type sulfides of the second- and third-row transition metals (RuS_2, OsS_2 and IrS_2) with intermediate bulk M–S bond strengths were found to be the most active catalysts.

The topological theory of Bader et al. provides a rigorous definition of chemical bonds for all classes of molecules and solids.[7–9] This theory uses the total electron density $\rho(\boldsymbol{r})$ of a molecule or solid to determine its topology. This topology is characterized by its critical points (CPs): maxima, minima, and saddle points. These are points where the gradient vector field $\nabla\rho(\boldsymbol{r})$ vanishes, and they are classified by the ρ(r) curvatures or three eigenvalues λ_i ($i = 1, 2, 3$) of the Hessian matrix ($H_{ij} = {}^2\rho(\boldsymbol{r})/x_i x_j$).[7] In general, $\rho(\boldsymbol{r})$ exhibits local maxima only at the nuclear positions and a saddle point between each pair of bonded nuclei. The latter is called a bond critical point, and its presence is a necessary condition for the existence of a chemical bond.[7, 8] A unique pair of trajectories of the vector field $\nabla\rho(\boldsymbol{r})$ that originate at the bond critical point define a line that links the nuclei, along which the electron density is a maximum with respect to any other neighboring line. This is a bond path, and its presence is a necessary and sufficient condition for the existence of a bond.[8] Bond paths determine and characterize all atomic interactions in a given system. The connection between the topology of the electron density and the chemical and structural stability of isolated molecules is well established.[7] In particular, the strength of the bonding between a given pair of atoms in a molecule correlates with the values of the electron density at the bond critical point ρ_b.[7] A simple relationship between the binding energy and ρ_b in periodic solids was also reported.[10–12]

We carried out a systematic determination of the topology of $\rho(\boldsymbol{r})$ for pyrite-type TMSs (RuS_2, OsS_2, IrS_2, FeS_2, and NiS_2) in order to examine the connection between the topologically defined M–S bond and HDS activity. The electron densities were calculated with the WIEN-97[13] program by using a Kohn–Sham Hamiltonian, which includes the generalized gradient approximation developed by Perdew et al.[14] and an unrestricted scheme for obtaining spin-polarized wave functions. The topology of $\rho(\boldsymbol{r})$ was analyzed with a local version of the EXTREM program,[15] incorporated in the EXCUBO[16] program and adapted to WIEN-97. The TMS experimental cell parameters were used.[17] We located all CPs in the cells, and Figure 1 shows the three-dimensional CP positions in the pyrite-type crystals. There are four M nuclei per primitive cell, eight S nuclei, twenty-four M–S bond CPs (b_{MS}), four S–S bond CPs (b_{SS}), twenty-four ring CPs, and eight cage CPs. The $\nabla\rho(\boldsymbol{r})$ trajectories that originate at each of the four cages and terminate at a *b* CP, define an interatomic surface (Figure 2). The M and S atoms are bonded by sets of six and four such surfaces, respectively. In the middle of each surface, there is a *b* CP, and the parameters that characterize these CPs are listed in Table 1. The $\rho(b_{MS})$ values allow us to predict that the trend in M–S bond strength is Os > Ir > Ru > Fe > Ni. Note that exactly the inverse trend is observed for the $\rho(b_{SS})$ values, that is, the S–S bond strength increases as the M–S bond strength decreases. Additionally, the curvatures of $\rho(\boldsymbol{r})$ at *b* are intimately related to the nature of the chemical bond.[18] The two negative curvatures λ_1 and λ_2 are connected to the perpendicular contraction of $\rho(\boldsymbol{r})$, which leads to a contraction of charge towards *b*. The positive curvature λ_3 is related to the parallel expansion of $\rho(\boldsymbol{r})$ and cause its depletion away from *b*. In a covalent bond[18] the negative curvatures dominate ($|\lambda_1 + \lambda_2| > \lambda_3$), so the electronic charge is concentrated in the internuclear region, and $\rho_b > 0.1$. In ionic bonds[18] the positive curvature dominates ($|\lambda_1 + \lambda_2| < \lambda_3$), so the electronic charge is depleted away from the internuclear region, and $\rho_b < 0.1$. The data listed in Table 1 show that the S–S bonds exhibit characteristics associated with a covalent nature, while the M–S bonds possess values typical of ionic or polar covalent bonds. A contour map of the Laplacian distribution[19] (Figure 3) corroborates that the M–S bonds correspond to the interaction of a relatively hard core of density on M with a softer, more polarizable region of charge concentration dominated by contractions of $\rho(\boldsymbol{r})$ towards the b_{SS} CP. Examination of Figures 2 and 3 reveals that sulfur atoms

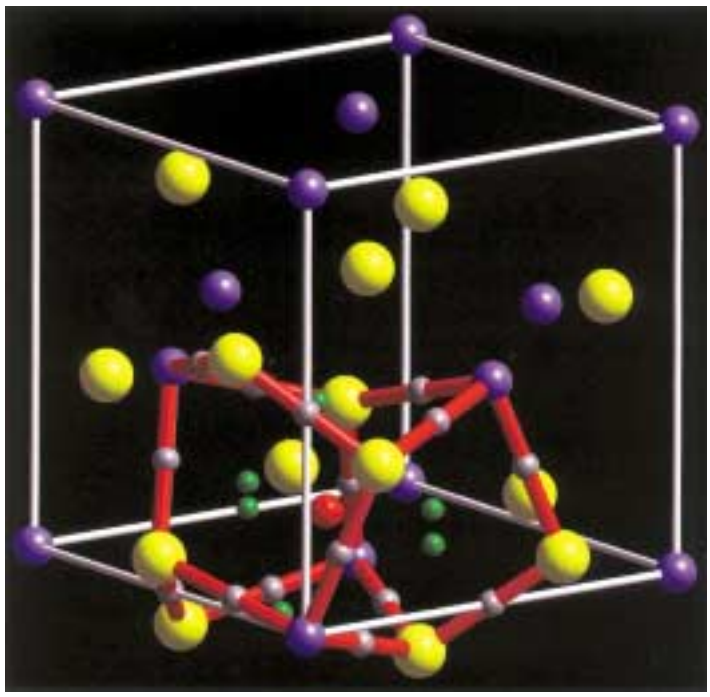

Figure 1. $\rho(\boldsymbol{r})$ critical points in the unit cell (white cube) of RuS_2. Blue and yellow spheres represent Ru and S atoms, respectively. Red rods denote the bond paths defined by the bond critical points (gray spheres). Only one cage critical point (red sphere), defined by a six-face polyhedron, is shown. Green spheres denote the five-membered ring CPs.

  1433-7851/00/3921-3811 $ 17.50+.50/0

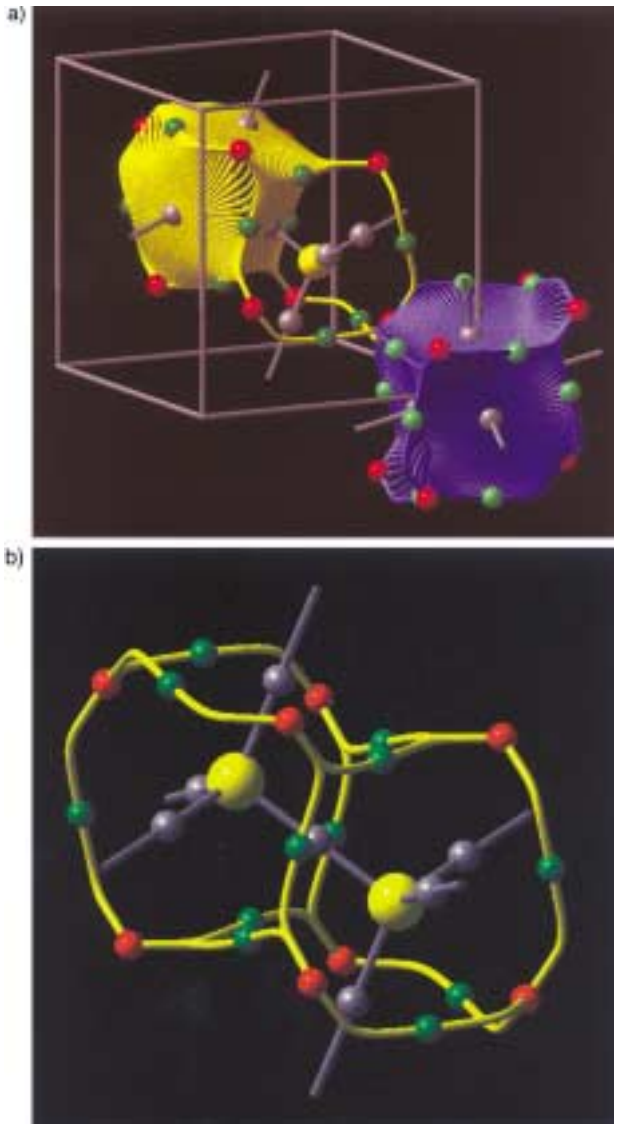

Figure 2. a) Representation of the region of space bounded by the six and four interatomic surfaces that define a Ru atom (blue zone) and an S atom (yellow zone), respectively. b) An S_2 group is defined by eight cage CPs (red spheres) and the surface perimeter is formed by the trajectories of the vector field $\nabla\rho(\boldsymbol{r})$ (yellow lines) originating at the cage points and ending at the ring points (green spheres). Bond paths (gray rods) to six metal atoms link each S_2 group.

Table 1. Topological properties (au) of $\rho(\boldsymbol{r})$ at the critical points for bulk pyrite-type transition metal sulfides.

Critical point	$\rho(\boldsymbol{r}_c)$	λ_1	λ_2	λ_3
		RuS_2		
b_{MS}	0.09030	−0.07197	−0.06931	0.32877
b_{SS}	0.12498	−0.14805	−0.14805	0.22292
		OsS_2		
b_{MS}	0.09905	−0.07180	−0.06771	0.32877
b_{SS}	0.11680	−0.13738	−0.13738	0.22292
		IrS_2		
b_{MS}	0.09580	−0.07745	−0.07748	0.28627
b_{SS}	0.11901	−0.13768	−0.13768	0.23730
		FeS_2		
b_{MS}	0.07903	−0.04604	−0.04372	0.27775
b_{SS}	0.13251	−0.15756	−0.15756	0.20880
		NiS_2		
b_{MS}	0.06574	−0.04715	−0.04679	0.20889
b_{SS}	0.14745	−0.16544	−0.16544	0.17789

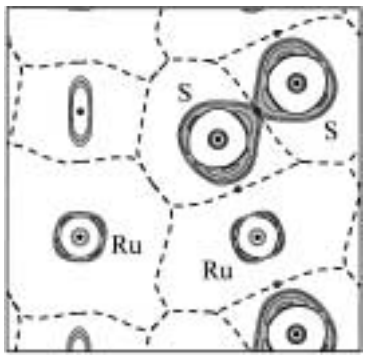

Figure 3. Contour map of $\nabla^2\rho$ on the (110) plane for bulk RuS_2. The contours denote negative values of $\nabla^2\rho$, that is, concentration of electronic charge (shaded zones). The outermost contour is 0.0 and indicates the surface that separates the charge-concentration zone from the outer, charge-depletion zone. Dotted lines mark the intersection of the interatomic surfaces with the plane of the figure. The map shows that S_2 dimers are linked to the metal atoms.

form covalently bonded S–S groups which assemble about a metal atom. Thus, the pyrite-type TMS crystal packing results from the interaction of each metal atom with six such S_2 groups.

The HDS activity of TMSs has been related to the ability of the catalyst to form and regenerate sulfur vacancies,[2, 3] that is, to the breaking of M–S bonds. The model developed by Topsøe et al.[2] suggests that the highest HDS activities correspond to the TMSs with the lowest M–S bond strength (RuS_2, OsS_2, and IrS_2), that is with the lowest $\rho(b_{MS})$ value. However, sulfides of second- and third-row transition metals show $\rho(b_{MS})$ values greater than those of sulfides of first-row metals (Table 1). This result is in contrast with the above model. To further study the HDS behavior of TMSs, we also calculated $\rho(b_{MS})$ for the less active compounds VS, FeS, MnS, and PtS.[20] We observed that $\rho(b_{MS})$ shows exactly the same trend (Pt > Ir > Os > Ru > V > Fe > Mn) of the M–S bond strength as was reported by Toulhoat et al.[5] The variation of the HDS activity with $\rho(b_{MS})$ is shown in Figure 4. Like

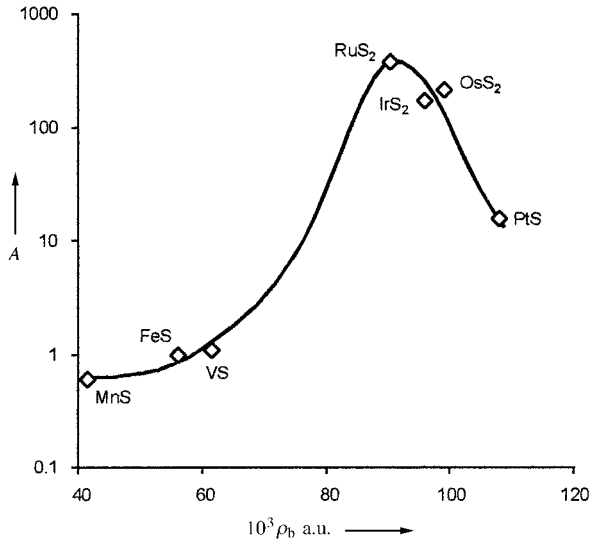

Figure 4. HDS activity A (10^{16} molecules of DBT converted per mmole metal per second)[3] of the TMS catalysts as a function of the electron density at the metal–sulfur bond critical point.

  1433-7851/00/3921-3812 $ 17.50+.50/0

Toulhoat et al., we found the typical volcano plot. It is evident that TMSs with either too high or too low $\rho(b_{MS})$ values possess only low HDS activity. The most active catalysts are characterized by intermediate values of the electronic density at the M–S bond critical point. This result corroborates, by means of a bond concept that is rigorously defined by the topological theory of $\rho(\boldsymbol{r})$, the consistency of TMS-catalyzed HDS with the Sabatier principle.

Received: April 13, 2000
Revised: June 13, 2000 [Z14987]

[1] O. Weisser, S. Landa, *Sulfide Catalysts: Their Properties and Applications*, Pergamon, Oxford, **1973**.
[2] H. Topsøe, B. S. Clausen, F. Massoth, *Hydrotreating Catalysis* in *Catalysis, Science and Technology, Vol. 11*, Springer, Berlin, **1996**.
[3] T. A. Pecoraro, R. R. Chianelli, *J. Catal*. **1981**, *67*, 430.
[4] J. K. Norskov, B. S. Clausen, H. Topsøe, *Catal. Lett*. **1992**, *13*, 1.
[5] P. Raybaud, G. Kresse, J. Hafner, H. Toulhoat, *J. Phys. Condens. Matter* **1997**, *9*, 11085; H. Toulhoat, G. Kresse, *Abstr. Pap. Symp. on Advances and Applications of Computational Chemical Modeling to Heterogeneous Catalysis* (New York: American Chemical Society) **1997**, p. 114.
[6] P. Sabatier, *Ber. Dtsch. Chem. Ges*. **1911**, 44; M. Boudart, *Chem. Eng. Prog*. **1961**, *57*, 33.
[7] R. F. W. Bader, *Atoms in Molecules—A Quantum Theory*, Clarendon, Oxford, UK, **1990**.
[8] R. F. W. Bader, *J. Phys. Chem*. **1998**, *102*, 7314.
[9] R. F. W. Bader, P. L. A. Popelier, T. A. Keith, *Angew. Chem*. **1994**, 106, 647; *Angew. Chem. Int. Ed. Engl*. **1994**, *33*, 620.
[10] P. Zou, R. F. W. Bader, *Acta Crystallogr. Sect. A* **1994**, *50*, 714.
[11] V. Luaña, M. A. Pendás, A. Costales, *Phys. Rev. B* **1997**, *55*, 4285.
[12] Y. Aray, J. Rodriguez, D. Vega, *J. Phys. Chem. B* **2000**, *104*, 4608.
[13] P. Blaha, K. Schwarz, J. Luitz, *WIEN 97*, Vienna University of Technology **1997**. (Improved and updated Unix version of the original copyrighted WIEN code: P. Blaha, K. Schwarz, P. Sorantin, S. B. Trickey, *Compt. Phys. Commun*. **1990**, *59*, 399.)
[14] J. P. Perdew, S. Burke, M. Ernzerhof, *Phys. Rev. Lett*. **1996**, *77*, 3865.
[15] R. F. W. Bader, P. Krugg, Department of Chemistry, McMaster University, Hamilton, Ontario, Canada, **1990**, personal communication.
[16] Y. Aray, J. Rodriguez, J. Rivero, *J. Phys. Chem*. **1997**, *101*, 6976.
[17] RuS_2: H. D. Lutz, B. Mueller, T. Schmidt, T. Sting, *Acta Crystallogr. Sect. C* **1990**, *46*, 2003; OsS_2: T. Sting, B. Mueller, H. D. Lutz, *Z. Kristallogr*. **1992**, *202*, 161; IrS_2: E. Parthé, D. Hohnke, F. Hulliger, *Acta Crystallogr.* **1967**, *23*, 832; FeS_2: S. Finklea, C. Leconte, E. Amma, *Acta Criystallogr. Sect. B* **1976**, *32*, 529; NiS_2: T. Fuji, K. Tanaka, F. Marumo, Y. Noda, *Mineral. J. Jpn*. **1987**, *13*, 448.
[18] R. F. W. Bader, H. J. Essen, *J. Chem. Phys.* **1984**, *80*, 1943; S. Grimme, *J. Am. Chem. Soc.* **1996**, *118*, 1529.
[19] A contour map of the Laplacian $\nabla^2\rho$ (the sum of the three curvatures at each point in space) allows us to see the extent and relative position of the regions where electronic density is concentrated ($\nabla^2\rho < 0$) or depleted ($\nabla^2\rho > 0$). In a covalent bond, the electron density is concentrated between the nuclei, around the bond critical point (ref. [7] and "The Laplacian of the Electronic Charge Distribution": P. J. MacDougall, PhD Thesis, McMaster University, Hamilton, Ontario, Canada, **1989**).
[20] Cell parameters: VS: W. Biltz, A. Koecher, *Z. Anorg. Allg. Chem*. **1939**, *241*, 324; FeS: J. M. D. Coey, H. Roux-Buisson, *Mater. Res. Bull*. **1979**, *14*, 711; MnS: T. Chattopadhyay, H. G. von Schnering, R. F. D. Stansfield, G. J. McIntyre, *Z. Kristallogr*. **1992**, *199*, 13; PtS: F. A. Bannister, M. H. Hey, *Miner. Mag. J. Mineral. Soc*. **1932**, *23*, 188.

Higher Adducts of C_{60} by Tether-Directed Remote Functionalization: X-Ray Crystal Structure and Reactivity of a Chiral Hexakis-Cyclopropanated Fullerene with all Addends Located along an Equatorial Belt**

Craig R. Woods, Jean-Pascal Bourgeois, Paul Seiler, and François Diederich*

Hexakis adducts of C_{60} are increasingly attracting interest as three-dimensional building blocks for advanced materials applications.[1, 2] Among those, derivatives with a pseudooctahedral (T_h) addition pattern have been the earliest and most widely investigated ones.[3–7] Recently, Rubin and co-workers reported the synthesis of a hexakis adduct with a novel, D_3-symmetric addition pattern, which features unusually strong fluorescence and electroluminescence properties.[1] Both types of hexakis adducts are accessible by stepwise additions and their addends are evenly distributed over the entire carbon sphere. In recent years, regio- and stereoselective tether-directed remote functionalization techniques[8] have provided access to a great variety of higher adducts of C_{60}, which either cannot be synthesized by stepwise additions or are obtained only in small yield from complex isomeric mixtures. Using such a methodology,[9] we became interested in preparing hexakis adducts with completely novel addition patterns, that feature the location of all addends along an equatorial belt rather than evenly distributed over the entire carbon sphere. In the chiral D_2-symmetric structure **A** (Figure 1) the addition sites are aligned in a distinct helical array,

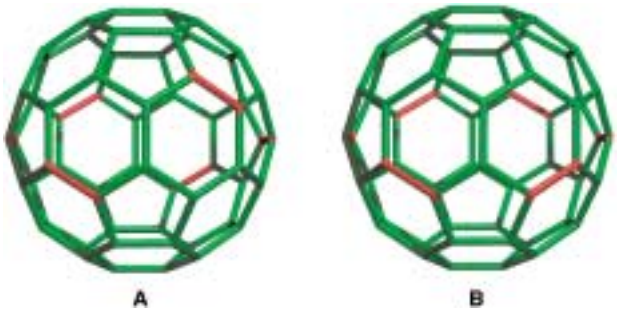

Figure 1. Novel hexakis addition patterns of C_{60} with the addend sites located along an equatorial belt.

whereas structure **B**, with a D_{3d}-symmetric addition pattern, features a circumferential ("Saturn"-like) functionalization about the equator which dissects the residual π-electron chromophore of the fullerene into two polar halves with no direct π-electron conjugation. Here, we report the synthesis,

[*] Prof. Dr. F. Diederich, Dr. C. R. Woods, Dipl.-Chem. J.-P. Bourgeois, P. Seiler
Laboratorium für Organische Chemie
ETH-Zentrum
Universitätstrasse 16, 8092 Zürich (Switzerland)
Fax: (+41) 1-632-1109
E-mail: diederich@org.chem.ethz.ch

[**] This work was supported by the Swiss National Science Foundation and the German Fonds der Chemischen Industrie

  1433-7851/00/3921-3813 $ 17.50+.50/0